Icarus xxx (xxxx) 114719

Contents lists available at ScienceDirect

Icarus

journal homepage: www.elsevier.com/locate/icarus

Seepage-evaporation controlled depletion of initially water-filled reservoirs on Earth and Mars: Analytic versus HYDRUS modeling

A.R. Kacimov [a,*], Yu.V. Obnosov [b], J. Šimůnek [c]

[a] Department of Soils, Water and Agricultural Engineering, Sultan Qaboos University, Oman
[b] Institute of Mathematics and Mechanics, Kazan Federal University, Kazan, Russia
[c] Department of Environmental Sciences, University of California Riverside, CA, USA

ARTICLE INFO

Keywords:
Surface water depletion by seepage from axisymmetric craters
Gardnerian soils and Wooding's unsaturated seepage from a shrinking disk
Hunt's phreatic saturated seepage from a dwindling paraboloidal cap
HYDRUS modeling of transient seepage from craters the water level in which evanesces

ABSTRACT

Analytical solutions are obtained for water extinction from an axisymmetric crater, filled at $t < 0$ and depleted by evaporation and transient infiltration into a Gardner or capillarity-free homogeneous soil during the time interval $0 \le t \le T_e$. The extinction time T_e is found for crater beds, the shapes of which are shallow cones, spherical, spheroidal, and paraboloidal caps. An instantaneous seepage flow rate, $Q(t)$, is approximated by truncated two-term formulae of Wooding for a zero-depth disk in Gardner's soil or Hunt for paraboloidal craters (soils with no capillarity). The instantaneous evaporation losses are the product of a constant A-pan evaporation rate and the shrinking area of a flat horizontal disk of the free water, which dwindles in the crater. In HYDRUS simulations of a van Genuchten soil, the Reservoir Boundary Condition is used for a falling water level in the ponded depressions. Cones and paraboloids are selected as craters, initially fully or partially filled with free water at $t = 0$, and infiltrating until extinction. The results are presented as drawdown curves and – for shallow craters - attest a good match between analytical approximations and HYDRUS numerical simulations. Experiments with the extinction of water from small axisymmetric ponds in dune sand are also carried out. They allow blitz-evaluation of hydraulic parameters of the subjacent sand. Hydrological implications for commingling surface-subsurface (pore) water entities in terrestrial and Martian environments are discussed.

List of abbreviations and notations

Symbol	Description	Unit
GA	Green-Ampt	–
PK-62, 77	Polubarinova-Kochina, P.Ya., 1962, 1977. Theory of Ground Water Movement.	–
VG	Van Genuchten	–
B	Ponded water depth in the crater	cm
θ	Volumetric soil water content	[–]
θ_r	Residual water content	[–]
θ_s	Saturated water content (porosity)	[–]
K_s	Saturated hydraulic conductivity	cm/h
n, α	VG soil parameters	[–], cm^{-1}
α_P	Sorptive number	cm^{-1}
p	Pressure head	cm
h	Total (piezometric) head	cm
t	Time	h
r	Radial coordinate	cm
z	Vertical coordinate	cm
V	Volume of free water in the pond	cm^3

"That last day does not bring extinction to us, but change of place."
Marcus Tullius Cicero

1. Introduction

Water in all forms (surface water, groundwater, liquid soil moisture, ice, and vapor in both atmosphere, on the land surface, and inside the pore space) and all types of its transport in the hydrological cycle (runoff, seepage, infiltration, deep percolation, groundwater motion, evaporation, precipitation) is of paramount importance for all human activities (agriculture, civil engineering, etc.). Recent irrefutable NASA discoveries of water on the Moon and Mars and other planets and their satellites in the Solar system determine the long-term strategies of conquering Space. The hydrology, hydrogeology, hydrogeochemistry, sedimentology, soil physics-mechanics of hyperarid deserts on the Earth serve as proving grounds to infer the physical properties of the liquid,

* Corresponding author.
E-mail addresses: anvar@squ.edu.om (A.R. Kacimov), yobnosov@kpfu.ru (Yu.V. Obnosov), jsimunek@ucr.edu (J. Šimůnek).

https://doi.org/10.1016/j.icarus.2021.114719
Received 10 December 2020; Received in revised form 14 September 2021; Accepted 21 September 2021
0019-1035/

solid, and gaseous phases of these planets. This will facilitate the forthcoming space missions and elucidate the past geological epochs of, say, Mars in backward modeling-reconstructions (see, e.g., Davila et al., 2021, Groemer et al., 2020).

In this paper, we extend our analytical and numerical studies of transient 2-D seepage from canals and "dry wells" (Al-Shukaili et al., 2019, 2020; Kacimov et al., 2020, 2021; Sasidharan et al., 2018) to axisymmetric flows from non-cylindrical reservoirs with water levels falling due to seepage into terrestrial/Martian soils and evaporation into the atmosphere. Interaction (exchange) between surface and subsurface waters has been thoroughly investigated in hydrology, limnology, soil physics, geomorphology, and other Earth sciences (see, e.g., Sophocleous, 2002, Woessner, 2020). Paleodynamics of depletion of the free water storage in Martian lakes/reservoirs came to space scientists' attention upon NASA indagation and the dazzling, albeit so far by remote sleuthing, discovery of deep groundwater (e.g., by a GPR technique). Mathematical modelers also started to portray the topology of Darcian seepage in Martian aquifers. In the current purview of the subdiscipline of Martian hydrology, a hypothesized dynamics of surface water in lakes, channels, and other fluvial or lacustrine entities is commingled with saturated Darcian flows (Baum and Wordsworth, 2020, Bhardwaj et al., 2019, Boatwright and Head, 2019, Fukushi et al., 2019, Goldspiel and Squyres, 2011, Grimm et al., 2014, 2017, Hobbs et al., 2014, Kochel and Piper, 1986, Luo et al., 2011, Kereszturi et al., 2010, Malin and Carr, 1999, Malin and Edgett, 2000, Marra et al., 2014, 2015, Michalski et al., 2013, Mukherjee et al., 2020, Salese et al., 2019). The commonality of landforms on Mars and Earth, for instance, gullies or catchments' drainage networks, and the terrestrial scrutiny of the impact of Darcian flows on their evolution (see, e.g., Blank et al., 2009, Conway et al., 2019 versus Petroff et al., 2013) stimulate further studies of subsurface mechanics on the two planets.

Soil physics of infiltration, deep percolation, groundwater motion in unconfined aquifers and the capillary fringe above the water tables, evaporation, redistribution, root water uptake, runoff, phase changes of pore water (including freezing-thawing and vapourization-condensation), and heat and solute transport in unsaturated porous media have been thoroughly studied, including validation of models via field and laboratory experiments, in terrestrial systems (Radcliffe and Šimůnek, 2010; Šimůnek et al., 2018). Without claiming a comprehensive review of the whole scope of reconnoitered extra-terrestrial Darican flows, it seems that the unsaturated and tension-saturated water (brine) flows on Mars (including the vadose zone and capillary fringe) have been ignored in mathematical models, i.e., the porous Martian media were posited capillarity-free. Only recently, qualitative statements about the role of capillarity have emerged: "*It is possible that a change in soil permeability might affect the local capillary rise and thus the surface visibility*" (Lark et al., 2020). Neglecting capillarity is reasonable for large Martian craters and mega-channels. However, for the forthcoming human missions to Mars and the realization of Tsiolkovsky-Mask's projects (populating Mars and other planets/satellites), a prodigious interest to apposite models of infiltration and saturated-unsaturated seepage from small-size man-made excavations, temporarily filled with water, is emerging. For example, human colonies on Mars may dispose of sewage in Martian lagoons. The astro-physio-hydro-biological question will then arise: how fast do the impounded-trickled liquids percolate-evaporate in the triad of Martian sediments-rocks-atmosphere? Upon comparisons of the above referenced Darcian models, used by Martian hydrologists, with the legacy of terrestrial irrigation-drainage sciences and engineering (Kacimov et al., 2020), we deem that several aspects of transient seepage still deserve to be unearthed.

Let us introduce the pore pressure, P, $P = \rho g p$, where p [cm][1] is the pressure head, ρ [g/cm^3] is liquid's (water, brine, oil, etc.) density, and g [cm/s^2] is gravity acceleration. Obviously, ρ is planet-invariant, and $g = 981$ and 371 cm/s^2 on Earth and Mars, respectively. We use the terrestrial acceleration in all our computations below (rescaling to Mars or other gravitating entities is straightforward, *modulo g)*.

In this paper, we consider axisymmetric groundwater and vadose zone motion, which obeys the Richards-Richardson equation:

$$\frac{\partial \theta}{\partial t} = \nabla (K(p) \nabla h) \tag{1}$$

where ∇ is the nabla operator in cylindrical coordinates, $\theta(t, r, z)$ is a volumetric water content [−], $K(p)$ [cm/h] is the hydraulic conductivity function, $h(t, r, z) = p + z$ is the total (piezometric) head [cm], z is a vertical coordinate oriented upward. It is well-known (Polubarinova-Kochina, 1962, 1977, hereafter abbreviated as PK-62,77, Strack, 2017) that the intrinsic permeability, $\kappa = K\mu/(\rho g)$ [cm^2], where μ [cP] is fluid's dynamic viscosity, as well as the capillary pressure function $p(\theta)$ (*modulo* sign, equivalent to the water retention function), and relative water permeability, $\kappa(\theta)$, depend on the properties of the porous skeleton only (provided water and air, as two fluids occupying the pore space, are fixed). The two functions are invariants in the whole Solar System (*modulo g*-rescaling).

We present analytical and numerical solutions to boundary value problems for eq. (1), which is coupled with the depletion of the storage of hydrostatically modeled water in a surface pond (crater). This interaction of surface-subsurface water brings about a new (Reservoir) boundary condition for axisymmetric flows, implemented recently in HYDRUS (Šimůnek et al., 2018), which accounts for a falling head problem for reservoirs of different shapes. This condition was analytically involved in 1-D seepage flows (Philip, 1992) and 2-D flows in a vertical plane (Al-Shukaili et al., 2020).

The results of this paper will outreach to soil hydrologists and water resources managers working in arid zones, where topographical depressions on Earth's surface are temporarily filled by episodic rains or irrigation events (e.g., sprinkling over crop fields). For example, the 2018 Mekunu cyclone caused torrential rains in the dune fields of the hyper-arid Empty Quarter in Oman and Saudi Arabia, with large interdunal valleys converted into ephemeral lakes. For local Bedouins confronting exiguous water sources, a vital question was: How long can the pond be utilized as an ephemeral oasis to provide drinking water for camels? The longer, the better. At the instance when the extant surface water vanishes, groundwater pumping has to start providing water supply to the cattle. However, the infiltrated water may still percolate through a vadose zone before reaching a deep aquifer from which pumping is feasible. Environmentally opposite abject scenarios emerge in illegal-clandestine dumping of toxic liquid waste in depressions of desert sand or wadis. To detect and catch the dumping criminals, the slower infiltration of the waste into the desert sand, the better. In the ensuing litigations, sampling of the extant liquid from a pond and comparing water quality in it with one in remote contaminated groundwater wells is the key evidence in forensic hydrology. For agronomists, ecohydrologists, and irrigation engineers, depletion of temporary static surface water bodies (owing to evaporation and infiltration) is also of utmost practical interest because a conjunctive use of water resources requires a smart alteration of operation of surface pumps and well pumps (like during the last 2011–2017 Big Drought in California). There is a fascinating analogy between soils-sediments-landforms-hydrology on Mars and in hot deserts of Earth (see, e.g., recent projects by space scientists in Oman and Israel: https://oewf.org/en/portfolio/amadee-20/; https://oewf.org/en/portfolio/amadee-18/ and Groemer et al., 2020).

2. Analytical solution for falling head Seepage from shallow axisymmetric ponds into Gardner's and capillarity-free soils

In an axial cross-section (Fig. 1a), a shallow axisymmetric reservoir is assumed to be filled with water. In an aerial view at $t < 0$, the

[1] The units are indicated solely for matching HYDRUS modeling below.

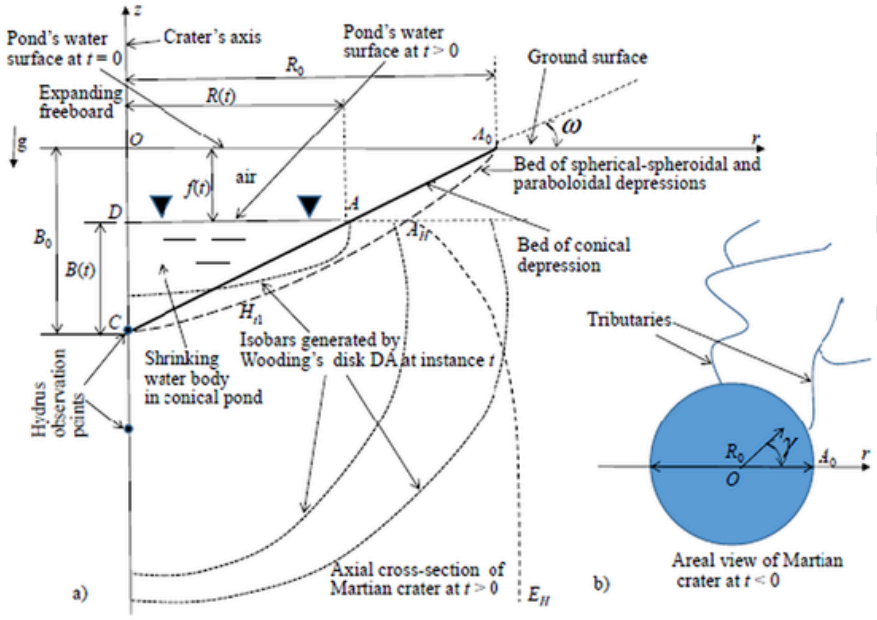

Fig. 1. a) Axial cross-section of a crater; b) aerial view of crater's disk on the Earth/Martian surface.

ponded surface represents a disk (Fig. 1b) of a radius R_0 [cm], which shrinks with time, such that the radius of a free water surface DA decreases as $0 < R(t) < R_0$. The extinction time, T_e, when surface water ponding ceases, i.e., $R(T_e) = 0$, is a part of the solution.

Without any loss of generality, we suppose that there is no freeboard in the pond at $t < 0$, i.e., the initial water level OA_0 is at the same horizon as the soil surface. This Section deals with four geometries of the pond's beds: conical, spherical, spheroidal, and paraboloidal. The soil of the crater bed is putatively homogeneous, isotropic, and either Gardnerian or capillarity-free. For the former, a dyad of soil hydraulic parameters is (K_s, α_P), where K_s [cm/day] is the saturated hydraulic conductivity, and α_P [1/cm] is the Philip sorptive number (see, e.g., Angulo-Jaramillo et al., 2016). Then in eq. (1), $K = K_s \exp.[\alpha_P p]$, $-\infty < p \le 0$. For the latter (a capillarity-free system), only K_s is needed to model seepage from the reservoir.

We also surmise that the soil extends indefinitely deep at $z < 0$, i.e., we follow Wooding (1968), Weir (1986), and Hunt (1973) in dealing with a porous half-space (without any confining substrata), into which seepage flow propagates. Strictly speaking, an unbounded porous half-space is a reasonable approximation for small-size reservoirs. Indeed, at large scales (on Earth, as well as on other planets and their satellites in the Solar System, e.g., Titan), the value of K_s decreases with depth (see, e.g., Horvath and Andrews-Hanna, 2021, Horvath et al., 2016, Rehbinder and Isaksson, 1998, Toller and Strack, 2019). Colmation of the bed is ignored, i.e., the contour CA_0 in Fig. 1a is a line along which the piezometric head is spatially constant at any fixed instance t.

2.1. Conical pond

The initial cone's depth, B_0 [cm] (Fig. 1a, solid line), obeys the inequality $R_0 >> B_0$, i.e., a bank slope $\omega = \arctan(B_0/R_0)$ is small. A straight line CAA_0 in Fig. 1a, which makes the cone by rotation around Oz, is $z = -B_0 + r \tan \omega$.

The origin, O, of a cylindrical coordinate system (z,r,γ) in Fig. 1a is at the center of the disk $r < R_0$, $z = 0$; the angular (azimuthal) coordinate γ vanishes from the analysis.

At $t < 0$, seepage from the crater was steady-state, constant values of R_0 and B_0 were maintained by a constant channel (runoff) inflow into the crater from its tributaries (Fig. 1b). At $t = 0$, the pond started to empty due to two draining factors: seepage and evaporation.

We note that Warren et al. (2021) studied a "reverse" process of extravasation of groundwater through the bottom of a water-filled Martian crater, albeit taking into account dynamics of axisymmetric surface water flow hydraulics downslope crater's rim. We ignore evaporation of liquid pore water into soil-atmosphere vapor, albeit on the time scale of post-extinction dynamics of a subsurface hydrological system, evaporation-sublimation becomes an important component of the Martian hydrological cycle (see, e.g., Baum and Wordsworth, 2020, Fukushi et al., 2019, Grimm et al., 2017, Lark et al., 2020).

During the time span $0 \le t \le T_e$, water is lost from a ponded surface such that

$$\lim_{t \to T_e} (R(t), B(t)) = (0, 0)$$

i.e., $R(T_e) = 0$, $B(T_e) = 0$.

The surface water storage in the pond is characterized by the volume V (cm^3) of the cone:

$$V(t) = \pi R^2(t) B(t)/3 = \pi \tan \omega R^3(t)/3 \quad (2)$$

The principle of mass conservation yields:

$$\frac{dV}{dt} = -E(t) - Q(t) \quad (3)$$

In eq. (3), $E(t) > 0$ [cm^3/h] are evaporation losses, which are proportional to the open area of the pond. Consequently,

$$E(t) = e \pi R^2 \quad (4)$$

where e [cm/h] is the evaporation rate (which we assume to be constant at $t > 0$). For assessment of seepage losses, $Q(t) > 0$ [cm^3/h], we adopt the Lembke method of successive steady states (PK-62,77), i.e., we assume that at any time $t > 0$ seepage from the pond attains a new steady state determined by pond's radius $R(t)$. Hydrological balances equations, analogous with ours eqns. (3)–(4), were used in Horvath and Andrews-Hanna (2021) and Warren et al. (2021).

In Subsections 2.1–2.3, we approximate Q for our dwindling reservoir (cone and spherical-spheroidal caps) by the Wooding (1968) formula, which is widely used in infiltrometry (see, e.g., Angulo-Jaramillo et al., 2016):

$$Q(t) = K_s \pi R^2(t) \left(1 + \frac{4}{\pi \alpha_P R(t)}\right) \tag{5}$$

In eq. (5), the pond's depth is assumed to be zero, and, therefore, Wooding's purely unsaturated seepage is posited. Strictly speaking, for real reservoirs, a saturated "bulb", bounded by an "inverted water table" under the bed of a non-zero depth $B(t)$ should be taken into account (see, e.g., Sophocleous, 2002, Warrick and Zhang, 1987) and the corresponding Q would be higher than that in eq. (5).[2]

We put eqns. (4) and (5) into eq. (3) and get an initial value problem for a nonlinear 1st order ODE:

$$\tan\omega \frac{dR}{dt} = -e - K_s - \frac{4K_s}{\pi \alpha_P R(t)}, \quad 0 \le t \le T_e \tag{6}$$

where T_e is to be found.

We introduce dimensionless quantities: $(R^*, B^*, z^*, r^*) = (R, B, z, r)\alpha_P$, $t^* = tK_s\alpha_P$, $e^* = e/K_s$ and drop "*" (for the sake of brevity). Then eq. (6) becomes:

$$\begin{aligned} \tan\omega \frac{dR}{dt} &= -\left(e + 1 + \frac{4}{\pi R(t)}\right), \quad 0 \\ &\le t \\ &\le T_e, \quad R_0 \\ &\ge R \\ &\ge 0. \end{aligned} \tag{7}$$

Eq. (7) resembles the Green-Ampt (GA) eq. (PK-62,77). ODE (7) separates and integrates:

$$t(R) = \tan\omega \left(\frac{4 \log\left[(4 + \pi(1+e)R)/(4 + \pi(1+e)R_0)\right]}{\pi(1+e)^2} - \frac{R - R_0}{1+e} \right), \tag{8}$$

Eq. (8) can not be resolved explicitly with respect to R. For GA infiltration, PK-62,77 elaborated asymptotics $R(t)$, which she derived from series expansions. We can apply a similar analysis to eq. (8).

Using the **ParametricPlot** routine of Wolfram's *Mathematica* Wolfram (1991), in Fig. 2 (left panel) we plot the curves $R(t)$ for tan $\omega = 0.1$, $e = 0.1$, and $R_0 = 1$, 0.6, and 0.2 (curves 1, 2, 3, respectively). The right panel demonstrates the extinction time T_e as a function of R_0 for tan $\omega = 0.1$ and $e = 1$.

2.2. Spherical crater

In this subsection, we consider ponds, the beds of which are spherical caps. The generating contour is depicted in Fig. 1a by a dashed-line CA_0. A water-filled spherical cap (half of it at an instance t is shaded inside CA_0OC in Fig. 1a) is made of a sphere of a radius R_s. We limit our analysis with the case of a circular arc, rotated with respect to the Oz axis, but centered at point O. The radius of the base of the cap at $t > 0$ is $0 \le R(t) \le R_0 \le R_s$. The case of the center of a generating circular arc, positioned above or below the Or axis in Fig. 1a, is mathematically acceptable. Physically, natural reservoirs having $R > R_s$ are hardly possible in loose unconsolidated Martian or terrestrial sediments/soils because the angles of repose of these media are never obtuse. For example, in Fig. 1a, the case of $\omega > 90^o$ would be physically extravagant.

The volume of the body of revolution of a quarter of a circular arc CA (Fig. 1a) with respect to the Oz axis is:

$$V_s(t) = \frac{1}{3}\pi \left(R_s - \sqrt{R_s^2 - R^2(t)}\right)^2 \left(2R_s + \sqrt{R_s^2 - R^2(t)}\right), \quad 0 \le t \le T_e \tag{9}$$

Similar to Subsection 2.1 and using eq. (9), the change of water storage in the shrinking cap is:

$$\frac{dV_s}{dt} = \frac{\pi R^3}{\sqrt{R_s^2 - R^2}} \frac{dR}{dt} \tag{10}$$

To the dimensionless quantities introduced in Section 2.1 we add $R_s^* = R_s\alpha_P$ (and drop the asterisk).

Then, substituting eq. (10) in the LHS of eq. (3) and using eqns. (4) and (5), we come to the Cauchy problem for the ODE, which governs the extinction of surface water:

$$\frac{dR}{dt} = -(\pi R(1+e) + 4)\frac{\sqrt{R_s^2 - R^2}}{\pi R^2}, \quad R(0) = R_0. \tag{11}$$

We integrate the initial value problem (11) and obtain:

$$t(R) = \frac{\sqrt{R_s^2 - R^2} - \sqrt{R_s^2 - R_0^2}}{1+e} - \frac{4}{\pi(1+e)^2}\mathrm{ArcTan}\frac{R_0\sqrt{R_s^2 - R_0^2} - R\sqrt{R_s^2 - R^2}}{R_s^2 - R_0^2 - R\sqrt{R_s^2 - R^2}} + \frac{16}{\pi\rho(1+e)^2}\log\left[\frac{(4 + \pi(1+e)R)\left(4R_0 + \pi(1+e)R_s^2 + \rho\sqrt{R_s^2 - R_0^2}\right)}{(4 + \pi(1+e)R_0)\left(4R + \pi(1+e)R_s^2 + \rho\sqrt{R_s^2 - R^2}\right)}\right],$$

where $\rho = \sqrt{\pi^2 R_s^2(1+e)^2 - 16}$. The inequality $\pi R_s(1+e) \ge 4$ must hold as a necessary solvability condition of eq. (11). This is a purely mathematical limitation, which pops up from the deficiency of our model, which in eq. (5) simplifies a real crater (in the approximation of its infiltration rate) to a flat disk.

The results of computation by eq. (12) are presented in Fig. 3 as $R(t)$ for $e = 0.1$ and $R_s = 1.5$, $R_0 = 1.5$, 1, 0.5 (curves 1–3, respectively). Obviously, the emptying of the hemispherical crater (curve 1) is the longest. The shallowest spherical cap in Fig. 3 (curve 3) demonstrates almost no relatively flat part of the $R(t)$ curve. All three curves in Fig. 3 have an almost vertical segment at t close to T_e. Graph on the right panel presents $T_e(R_0)$ for $R_s = 1.5$ and $e = 1$.

2.3. Spheroidal crater

A spheroidal crater is obtained by the revolution of an ellipse $r^2/b^2 + z^2/c^2 = 1$ about the Oz-axis in Fig. 1a. As in the case of a spherical cap in Section 2.2, the center of the generating ellipse coincides with the origin of coordinates, and the slope of the bank of the crater at $t = 0$ does not exceed 90°. The two semi-axes of this ellipse are b and c. The shrinking radius DA in Fig. 1a is $R(t) \le R_0 \le b$. Additional dimensionless quantities are: $(b^*, c^*) = (b, c)\alpha_P$. Obviously, the case of a spherical cap is a particular case of spheroidal caps.

Similarly to Subsections 2.1–2.2 (the algebra is omitted), we get the following expression for the surface water storage in the pond:

[2] Seepage from ponds of non-zero depth will be numerically modeled by HYDRUS in Section 3.

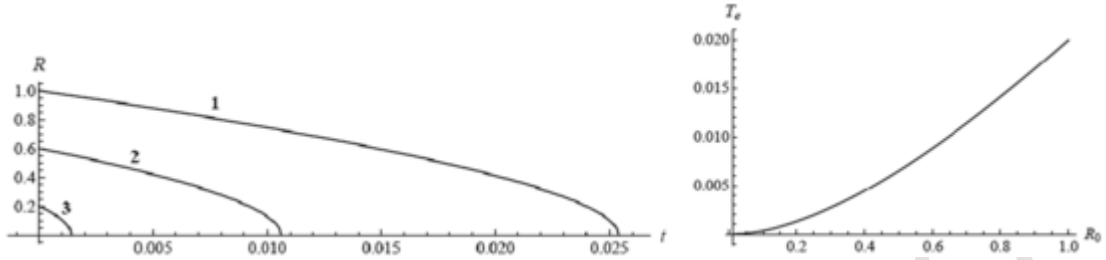

Fig. 2. Radius $R(t)$ of the surface water disk for conical ponds having $\tan\omega = 0.1$, and $R_0 = 1$, 0.6, and 0.2 (left panel curves 1, 2, 3, respectively), evaporation rate $e = 0.1$ (left panel); extinction time T_e (R_0) for a conical crater with $\tan\omega = 0.1$ and $e = 1$ (right panel).

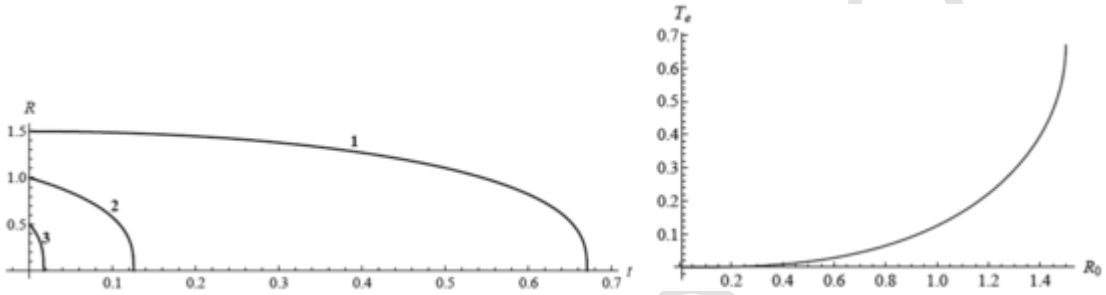

Fig. 3. Shrinking radius of the disk $R(t)$ of a ponded spherical cap for $R_s = 1.5$, $e = 0.1$, and $R_0 = 1.5$, 1, 0.5 (curves 1, 2, 3, respectively, left panel); extinction time T_e (R_0) for ponds made by a spherical cap having $R_s = 1.5$; surface water is subject to evaporation $e = 1$ (right panel).

$$V(t) = \frac{\pi c}{3b}\left(b - \sqrt{b^2 - R^2(t)}\right)^2 \left(2b + \sqrt{b^2 - R^2(t)}\right), \quad 0 \le t \le T_e. \tag{13}$$

Its rate of change, expressed via the time derivative of Wooding's disk, is:

$$\frac{dV}{dt} = \frac{\pi c R^3(t)}{b\sqrt{b^2 - R^2(t)}}\frac{dR}{dt} \tag{14}$$

The mass-balance (Cauchy's problem) is:

$$\frac{dR}{dt} = -\frac{b\sqrt{b^2 - R^2(t)}}{\pi c R^2(t)}\left((1+e)\pi R(t) + 4\right), \quad R(0) = R_0. \tag{15}$$

Analytical integration of ODE (15) yields:

$$t(R) = \frac{c}{b}\left(\frac{\sqrt{b^2 - R^2} - \sqrt{b^2 - R_0^2}}{1+e} - \frac{4}{\pi(1+e)^2}\mathrm{ArcTan}\frac{R_0\sqrt{b^2 - R_0^2} - R\sqrt{b^2 - R^2}}{b^2 - R_0^2 - R^2}\right) - \frac{16c}{\pi\rho b(1+e)^2}\log\left[\frac{(4+\pi(1+e)R)\left(\pi(1+e)b^2 + 4R_0 + \rho\sqrt{b^2 - R_0^2}\right)}{(4+\pi(1+e)R_0)\left(\pi(1+e)b^2 + 4R + \rho\sqrt{b^2 - R^2}\right)}\right], \tag{13}$$

where $\rho = \sqrt{\pi^2 b^2 (1+e)^2 - 16}$. A necessary condition for the solvability of eq. (15) is $\pi b(1 + e) \ge 4$.

Using eq. (15), in Fig. 4 (left panel) we plotted $R(t)$ for $b = 2$, $c = 1$, $e = 0.1$, and $R_0 = 2$, 1.5, 1 (curves 1, 2, 3, respectively). Similar to Fig. 3, the longest extinction and a pronounced relatively flat segment of the $R(t)$ curve in Fig. 4 is for the deepest crater, viz. a hemispheroid (curve 1). Fig. 4 (right panel) shows T_e (R_0) plotted for the same b, c, and e.

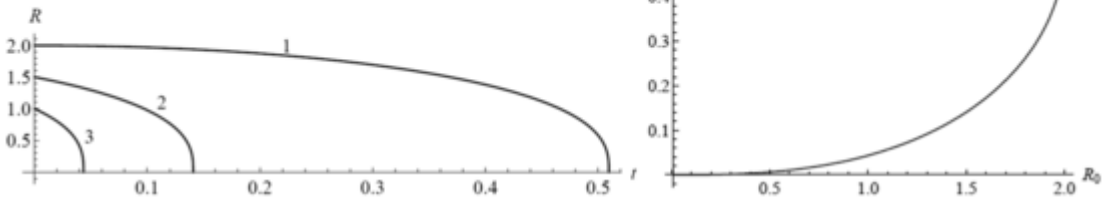

Fig. 4. Shrinking radius $R(t)$ of a ponded spheroid for $b = 2$, $c = 1$, $e = 0.1$, and $R_0 = 2$, 1.5, 1 (left panel, curves 1-3, respectively); extinction time for a spheroidal pond at $b = 2$, $c = 1$, and $e = 0.1$ (right panel).

2.4. Paraboloidal crater

Al-Shukaili et al. (2020) ignored the soil's capillarity in their analytical study of the extinction of ponded water from a triangular channel. In this subsection, we consider an evanescing ponding in a shallow paraboloid and also ignore capillarity. Thus, a generating curve CA_0 in Fig. 1a is a parabola:

$$z = B_0\left[(r/R_0)^2 - 1\right], \tag{17}$$

where $\varepsilon = B_0/R_0$ is Hunt's (1973) small parameter. The tip of the parabola is $z = -B_0$. For the freeboard $f(t) > 0$ in Fig. 1a, we have $f(0) = 0$ and $f(T_e) = B_0$.

The instantaneous volume of ponded water is

$$\begin{aligned} V(t) &= \pi\int_{-B_0}^{-B_0+B(t)} r^2(z)\,\mathrm{d}z \\ &= \pi R_0^2\int_{-B_0}^{-B_0+B(t)}\left(1+z/B_0\right)\mathrm{d}z \\ &= \frac{\pi R_0^2 B^2(t)}{2B_0} \\ &= \frac{\pi B_0 R^4(t)}{2R_0^2} \end{aligned} \tag{18}$$

Eq. (30) from Hunt (1973) is used to calculate instantaneous seepage losses from a shrinking paraboloidal pond. In this equation, we select Hunt's (1973) parameters b = c = 0 and a = 1 that in our notations yields:

$$Q(t) = \pi K_s R^2(t)\left[1 + 1.29B_0R(t)/R_0^2\right] \tag{19}$$

Note that at any instance $0 \le t \le T_e$, Hunt's seepage is bounded by a phreatic line A_HE_H (Fig. 1a), above which soil is instantaneously drained (no capillarity). In other words, the flow domain is a plume, which is bounded by a shrinking line A_HC where point A_H "slides" to point C as the time approaches T_e. The difference between Hunt's and Wooding's seepage models is discussed by Philip (1990).

We put eqns. (18) and (19) into eq. (3), keep the same eq. (4) in its RHS (viz. counting evaporation from the shrinking disk of the free water surface of our paraboloidal cap), and get:

$$\frac{\mathrm{d}V}{\mathrm{d}t} = \frac{2\pi B_0 R^3(t)}{R_0^2}\frac{\mathrm{d}R}{\mathrm{d}t} \tag{20}$$

The dimensionless quantities: $(R^*, B^*, z^*, r^*) = (R, B, z, r)/R_0$, $Q^* = Q/(K_sR_0^2)$, $V^* = V/R_0^3$, $t^* = tK_s/R_0$, $e^* = e/K_s$, $\varepsilon = B_0/R_0$ with omitted superscripts "*"s are used below. Eq. (19) is valid for relatively small ε.

Substitution of eqns. (20), (19), and (4) into eq. (3) leads to the Cauchy problem for the following ODE:

$$\frac{\mathrm{d}R}{\mathrm{d}t} = -\frac{1+e+1.29\varepsilon R}{2\varepsilon R}, \quad R(0) = 1 \tag{21}$$

Integration of a GA-type eq. (21) results in:

$$t(R) = \frac{2}{1.29}\left(1 - R + \frac{1+e}{1.29\varepsilon}\log\frac{1+e+1.29\varepsilon R}{1+e+1.29\varepsilon}\right) \tag{22}$$

Obviously, in eq. (22), $t(1) = 0$ and $t(0) = T_e$.

Fig. 5 illustrates the effect of evaporation: the left panel plots $R(t)$ according to eq. (22) for $\varepsilon = 0.1$ and $e = 0.1$, 0.4, and 0.7. The right panel of Fig. 5 illustrates the effect of the paraboloid's depth on the extinction time $T_e(\varepsilon)$ for $e = 0.1$.

3. HYDRUS modeling

In this Section, we use HYDRUS (2D/3D) (Šimůnek et al., 2018) for a numerical solution of an axisymmetric Richards' eq. (1) applied to the following shapes of the craters: a cone and paraboloidal cap. Below we present the details for the former body of revolution.

An axial cross-section is shown in Fig. 6. Due to symmetry, only half of the flow domain is presented as a pentagon OCA_0UEO. The origin of cylindrical coordinates Orz is at the bottom left corner of the pentagon. The sizes of the pentagon, L_h and L_v, are selected large enough for soil water to percolate freely and not to be constrained laterally by an artificial cylindrical boundary (a line UE in Fig. 6). We selected $L_h = 800$ cm and $L_v = 1000$ cm. The following sizes characterize the conical crater: $R_0 = B_0 = 1$ m, i.e., the bank slope is 45°. The water table at $t = 0$ is at the top of the transport domain (at the soil surface) (Fig. 1a), i.e., $f(0) = 0$.

Soil is made of the van Genuchten's (VG) non-hysteretic loam (see, e.g., Šimůnek et al., 2018), for which the soil hydraulic properties are (θ_r, θ_s, α, n, K_s) = (0.078, 0.43, 0.036 1/cm, 1.56, 24.96 cm/day). In HYDRUS, we selected the 2D-General type of geometry and 2D-Axisymmetric Vertical Flow. The total simulation time was $T_H = 60$ days (i.e., large enough to be greater than T_e). The initial condition at $t = 0$ was $p(0,r,z) = -1000$ cm.

The transport domain was discretized into an unstructured finite element mesh (Fig. 6) with a targeted size of finite elements of 32 cm and the mesh refinement of 5 cm on the CA_0 boundary, which resulted in 2374 finite element nodes, 171 1D elements, and 4575 2D elements (triangles). The default HYDRUS iteration criteria were used. The segments OC and UE were no-flow boundaries, and OD was a free drainage boundary. We assumed that the segment A_0U was also a no-flow boundary, although evaporation from this moist segment can be modeled in HYDRUS. Along the A_0C segment, a new HYDRUS **Reservoir Boundary Condition** (see Šimůnek et al., 2018; Sasidharan et al., 2018) with a **Furrow** reservoir type was used. Evaporation from the open water body AD was also neglected.

Fig. 7 (left panel) shows HYDRUS-computed water depth for the conical project depicted in Fig. 6. All water infiltrated in 1.35 days. Fig. 7 (right panel) presents a drawdown curve for $R_0 = 100$ cm,

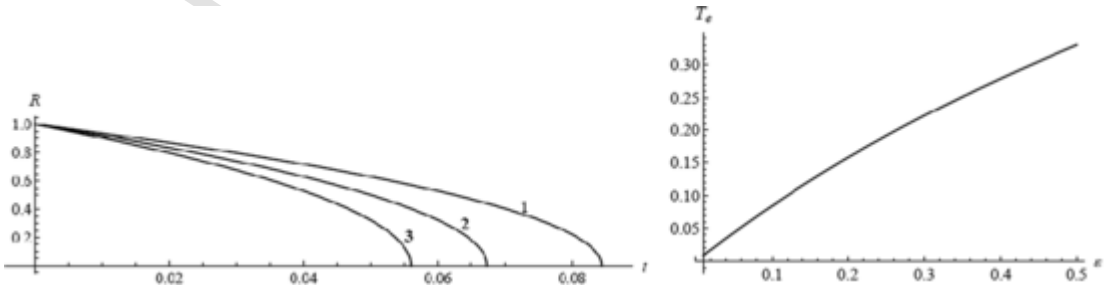

Fig. 5. The radius of the surface water disk $R(t)$ in a paraboloidal reservoir for $\varepsilon = 0.1$ and $e = 0.1$, 0.4, and 0.7 (left panel, curves 1-3, respectively); extinction time $T_e(\varepsilon)$ in a paraboloidal reservoir for $e = 0.1$.

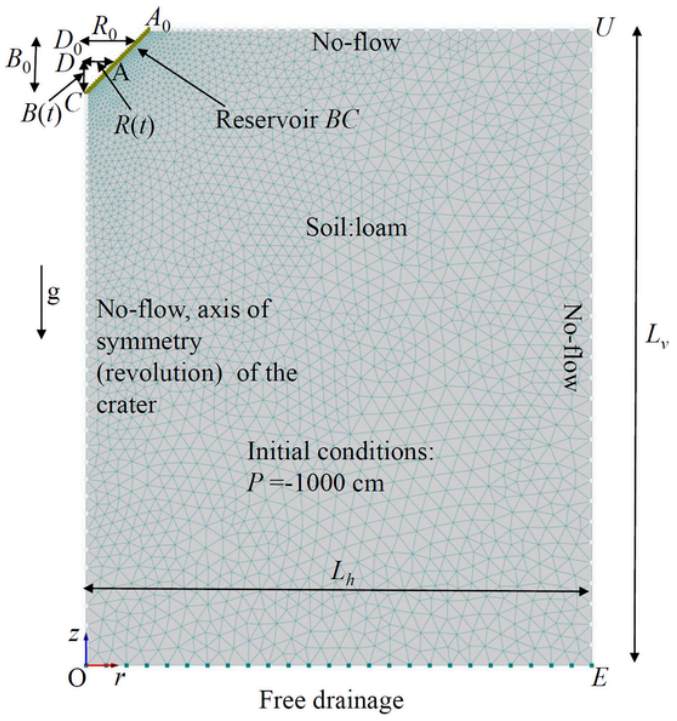

Fig. 6. The transport domain for a conical crater with its dimensions, initial and boundary conditions, and finite element mesh.

B_0 = 10 cm. The HYDRUS extinction time for this shallower cone is 0.25 days. To compare these results with analytical ones (i.e., eq. (8)), we convert α_P to α by the Ghezzehei et al. (2007) formula $\alpha_P = 1.3\alpha\ n$ that gives for the VG loam α_P = 0.076 1/cm. For the crater in Fig. 7, eq. (8), converted to dimensional quantities, gives T_e = 2.7 days, while for the bank slope ω = 0.1 the analytical value is T_e = 0.27 days. Therefore, for a deep cone, the Wooding analytical approximation (neglecting the reservoir depth) is inadequate. For shallow cones, there is a good match between HYDRUS results and eq. (8).

We notice a steep slope of the $B(t)$ curves in Fig. 7 at t close to T_e when only a small quantity of surface water remains in the cone (Al-Shukaili et al., 2020 got similar results for triangular channels). This is caused mainly by the convex shape of the $V(B)$ (water storage-water depth) function for cones and a much smaller increase in the water volume versus water depth (dV/dB) when water depths go to zero, compared to other geometrical shapes (spheroids, paraboloids). In our HYDRUS model, we placed an observation point C (Fig. 6) at the cone's tip and got the post-extinction limb of the $p(t)$ curve $-\infty < p(t) < 0$. In the range $-p_c < p(t) < 0$, where p_c is a soil-specific constant, capillarity stabilizes the excavation, i.e., the marcescent sediments on the slopes of the crater are temporarily upheld by moisture suction (too parched and too wet soils are less stable against liquefaction, and Aeolian and other types of erosion).

The paraboloidal cap was simulated for a much larger domain (L_h = 30 m and L_v = 25 m). The origin of cylindrical coordinates D_0rz is now at the top left corner of the transport domain. The paraboloidal cap was generated using a function $Z = br^2$ for b = 0.08 1/m and the origin of the paraboloidal cap, i.e., point C in Fig. 6, shifted to $z = Z - 8$ m. In this example, the cap's initial water table was 3 m below the soil surface ($f(0)$ = 3 m), i.e., the initial water depth B_0 = 5 m. The width of the paraboloidal cap at the soil surface is R_0 = 10 m.

Similarly, as above, the soil is made of the VG non-hysteretic loam. The total simulation time was T_H = 50 days (i.e., large enough to be greater than T_e). The initial condition at t = 0 was $p(0,r,z) = -10$ m.

The transport domain was discretized into an unstructured finite element mesh with a targeted size of finite elements of 0.1 m, a stretching factor of 4 (larger elements in the horizontal direction), the mesh refinement of 0.025 m on the CA_0 boundary, the mesh refinement of 0.2, 0.25, and 0.2 m in the corner nodes O, E, and U, respectively, which resulted in 9190 finite element nodes, 376 1D elements, and 18,002 2D elements (triangles). As above, evaporation from the soil surface or the water table was neglected. The **Reservoir Boundary Condition** (see Šimůnek et al., 2018, Sasidharan et al., 2018) with a **Paraboloidal** reservoir type was used along the A_0C segment.

Fig. 8 shows the HYDRUS-computed water depth for the paraboloidal cap. The extinction time is about 11 days. For comparisons, the analytical solution, eq. (22), gives for this paraboloid T_e = 14.16 days. In this example, capillarity again increases $Q(t)$ and decreases T_e. What are other factors affecting seepage? In analytical models of seepage from channels and reservoirs (free boundary problems for the Laplace equation, the Vedernikov-Bouwer model), the variational theorems (see, e.g., Ilyinsky et al., 1998) guarantee that if an isobaric drainage layer OE in Fig. 6 rises, then $Q(t)$ increases. Therefore, we surmise that the HYDRUS "free drainage" condition along OE in Fig. 6 also increases $Q(t)$ compared with Hunt's solution, for which this condition holds infinitely deep under the reservoir. On the other hand, the variational theorems (see, e.g., Ilyinsky et al., 1998) also rigorously prove that any artificial confinement of free-boundary seepage by an external no-flow surface, e.g., a cylindrical surface $r = L_h$, $0 < z < L_v$ in Fig. 6, reduces $Q(t)$ compared with both Hunt's laterally unbounded flow domains. HYDRUS calculates $Q(t)$ based on the Richards equation, and Wooding's Q would decrease if any impermeable boundaries confine the porous flow domain.

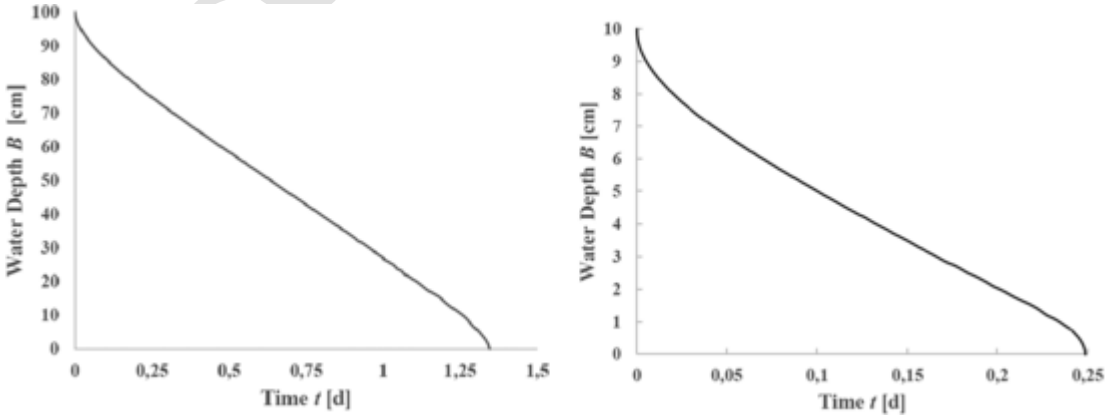

Fig. 7. The water depth B as a function of t in a conical crater simulated by HYDRUS: $R_0 = B_0$ = 100 cm (left panel) and R_0 =100 cm, B_0 = 10 cm (right panel). Note different scales on axes in the left and right figures.

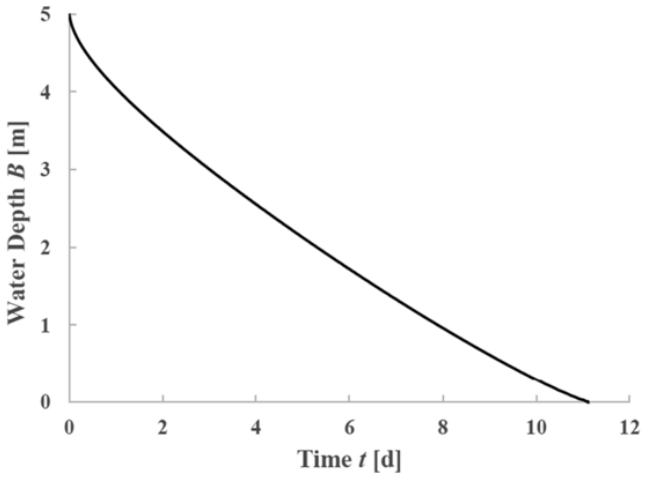

Fig. 8. The water depth B as a function of t in a paraboloidal cap simulated by HYDRUS.

Fig. 9 represents the results of HYDRUS computations for the same paraboloidal crater as in Fig. 8. The panels show a sequence of coloured maps of θ at five timeinstances: $t = 1$, 5, 10, 20, and 50 days. One can track, for example, evolution of a fully-saturated zone (the darkest red "bubble" bounded by an isohume $\theta = 0.43$). Specifically, at $t = 20$ days this zone separates from the bottom of an already empty crater while at $t = 50$ days this zone does not exist because capillarity has "devoured" the saturated "bubble". That means that a piezometer screened sufficiently deep under the crater will not detect any soil "wetting" signal $p > 0$.

4. Quick field experiments for infiltrometry

In October–November 2020, a series of experiments were conducted at the Agricultural Experimental Station (Sultan Qaboos University, Oman; N: 23°35′ E: 58° 9′). Excavations were shoveled in dry homogeneous dune sand (see the attached photo-video gallery of the experiments, Appendix 1). Several freshwater pulses of a temperature of 32–34° C were instantaneously poured into dug craters to stabilize their shapes and wet the subjacent sand, which is relatively coarse and permeable. After that, three liters of water were poured into a crater, and the radius $R(t)$ and the extinction time, T_{em}, were measured.

We present here the results for an initially water-filled crater having $B_0 = 6$ cm and $R_0 = 17$ cm. For this crater, $T_{em} = 1$ min 10 s. For such a short period of extinction, evaporation from DA in Fig. 1a can be neglected.

Using eq. (22) for this crater shape, we get dimensionless time $T_e = 0.27$. Therefore, $K_{se} = R_0 T_e / T_{em} = 3.9$ cm/min. Obviously, adjustment of K_s to other temperature values is needed using, for instance, the Hazen formula (PK-77).

Experimental errors are likely due to the crater's shape not being constant during infiltration. The poured surface water gyrates in the crater, scours the sand, and deposits it with small rills on the crater bed. The crater's shape is not exactly paraboloidal, and it is not easy to release the whole volume V_0 into the empty crater. Therefore, the instances $t = 0$ and T_{em} were not precisely measured. The experimentally found value of K_{se} is an overestimate of the real K_s because the used Hunt solution ignores capillarity.

There are, unfortunately, no analytical formulae for Q, even for steady-state flows, for axisymmetric seepage from ponds with free surfaces (capillary fringes or phreatic surfaces without capillarity). We can use an analogy with capillarity-counting seepage from soil channels (the Vedernikov-Bouwer model, see, e.g., Al-Shukaili et al., 2020, PK-62,77, Mahato and Dey, 2020). Indeed, for a Riesenkampf zero-depth channel with a width b_R and sand having an absolute value of h_c of the pressure head on the capillary fringe, the curve Q/Q_0 as a function of h_c/b is shown in Fig. 122 in PK-77. If we assume $b_R = 34$ cm and $h_c \sim 10 - 20$ cm, then $Q/Q_0 \sim 1.5 - 2.5$, i.e., if steady seepage losses from this channel are used for evaluation of K_s, then K_{se} will be overestimated by 50–150% for such a small crater. We surmise that for large ephemeral ponds and Martian craters (see, e.g., Bam et al., 2020), recorded emptying of these ponds will give K_{se} much closer to the actual K_s, as compared with mini-ponds reported in this Section. For terrestrial ponds, estimated K_s and Philip's sorptive number, α_P, or the van Genuchten dyad of (α, n), can be compared with HYDRUS simulations (see, e.g., Reynolds, 2015). This is similarly done for standard disc infiltrometers, which evaluate an allegedly steady-state unsaturated flow from a vertical burette through an isobaric discharge disk, with calculations of the dyad of (K_s,α_P) according to the Wooding formula. We also note that if the geometry of the crater and the whole flow domain are fixed, then for a constant value of K_s, capillary soils under steady-state flow conditions always have higher $Q(t)$ than soils without capillarity, whatever capillarity model (Gardner, van Genuchten, or Vedernikov-Bouwer with free boundaries) is selected. However, suppose soil's texture changes, i.e., both K_s and capillarity parameters vary. In that case, the impact on $Q(t)$ (and therefore T_e) is opposite: coarser soils have higher K_s but milder capillarity.

5. Concluding remarks

Wray (2021) wrote about the applicability of mathematical and physical models developed for terrestrial conditions to other planets, in particular, Mars: "…*alternative models often prove relevant in other planetary environments even if not in that for which they were first proposed.*" Cicero (see the epigraph) pointed out the link between the last day of extinction and the ensued change of the locus of an entity, which we interpret as a human soul or a finite initial volume of water V_0, stored hydrostatically at $t = 0$ in a reservoir. Such a pond can be a miniature terrestrial dimple on the surface of a crop field where local runoff is collected after an intense rainfall event (sprinkling irrigation), or a large Martian crater/lake, which suddenly loses its tributaries (Martian channels). Our analytical and HYDRUS modeling for saturated-unsaturated seepage from axisymmetric reservoirs predicts how fast water levels there drop with time. These results will serve to further optimize the shapes of the reservoirs via the solution of isoperimetric problems involving dynamics criteria, similar to Касимов and Тартаковский (1993). Also, the analysis of stable isotope enrichment of surface water and pore water recharging aquifers, when seepage losses are conjugated with seasonal evaporation, can be done for ephemeral ponds like those in Bam et al. (2020).

Our analytical and numerical models can be extended to the case of heterogeneous porous beds. In large-scale Martian studies of seepage (see, e.g., Horvath and Andrews-Hanna, 2021), the thickness of porous aquifers subjacent to large craters was several kilometers, and the hydraulic properties of these aquifers varied at kilometer scales. PK-62 pointed out that seepage losses of small-size earth channels are significantly reduced by colmation, which clogs few centimeters of the near-bed soil. Colmated craters/ponds can be easily modeled by HYDRUS, which can easily tackle two-component porous composites.

CRediT authorship contribution statement

A.R. Kacimov: Conceptualization, Methodology, Software, Formal analysis, Resources, Writing – original draft, Writing – review & editing, Visualization, Project administration, Funding acquisition. **Yu.V. Obnosov:** Conceptualization, Methodology, Software, Formal analysis, Writing – original draft, Writing – review & editing, Visualization. **J. Šimůnek:** Conceptualization, Methodology, Software, Formal analysis, Writing – original draft, Writing – review & editing, Visualization.

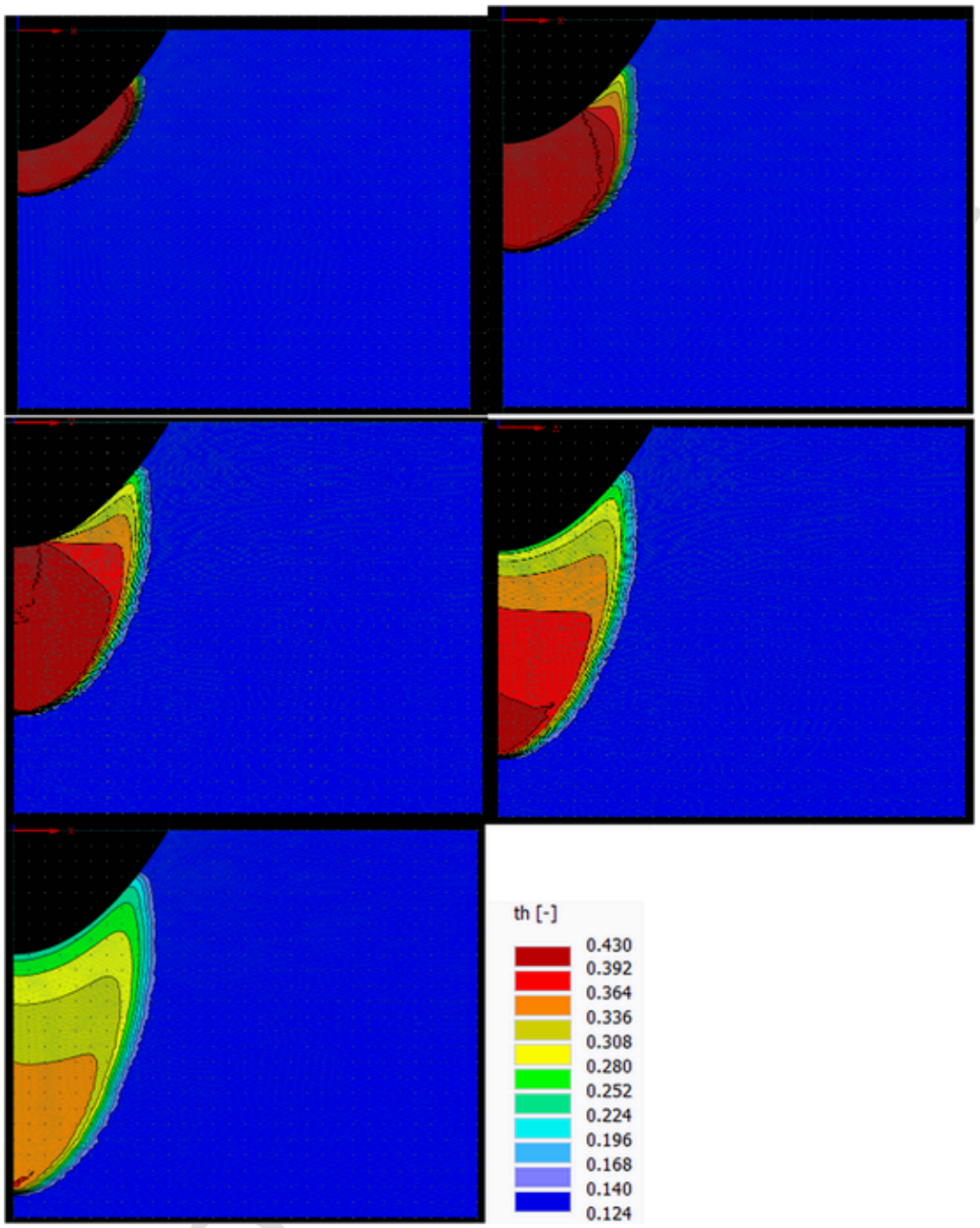

Fig. 9. HYDRUS–computed snapshots of the volumetric moisture content in an axial cross section for a paraboloidal cap in Fig. 8; time instances in the panels are $t = 1$, 5, 10, 20, and 50 days (left->right, up->down).

Declaration of Competing Interest

None.

Acknowledgments

This work was supported by the grants DR\RG\17 and IG/CAMS/SWAE/18/01, Sultan Qaboos University, Oman, and the development program of the Scientific and Educational Mathematical Center of the Volga Federal District, Russia, grant No. 075-02-2020-1478.

Appendix A. Supplementary data

Supplementary data to this article can be found online at https://doi.org/10.1016/j.icarus.2021.114719.

References

Al-Shukaili, A., Al-Mayahi, A., Al-Maktoumi, A., Kacimov, A.R., 2020. Unlined trench as a falling head permeameter: analytic and HYDRUS2D modeling versus sandbox experiment. J. Hydrol. 583, 124568. https://doi.org/10.1016/j.jhydrol.2020.124568.

Al-Shukaili, A., Al-Busaidi, H., Kacimov, A.R., 2019. Experiments, analytical and HYDRUS2D modeling of steady jet of quasi-normal surface flow in rectangular channel coupled with vertical seepage: Vedernikov-Riesenkampf's legacy revisited. Adv. Water Resour. 136, 103503.

Angulo-Jaramillo, R., Bagarello, V., Iovino, M., Lassabatere, L., 2016. Infiltration Measurements for Soil Hydraulic Characterization. Springer, Berlin.

Bam, E.K., Ireson, A.M., van der Kamp, G., Hendry, J.M., 2020. Ephemeral ponds: are they the dominant source of depression-focused groundwater recharge?. Water Resour. Res. 56 (3), e2019WR026640.

Baum, M., Wordsworth, R., 2020. Groundwater flow to Gale crater in an episodically warm climate. J. Geophysical Res. Planets 125 (8), e2020JE006397.

Bhardwaj, A., Sam, L., Martín-Torres, F.J., Zorzano, M.P., 2019. Are slope streaks indicative of global-scale aqueous processes on contemporary Mars?. Rev. Geophys. 57 (1), 48–77.

Blank, J.G., Green, S.J., Blake, D., Valley, J.W., Kita, N.T., Treiman, A., Dobson, P.F., 2009. An alkaline spring system within the Del Puerto Ophiolite (California, USA): a

Mars analog site. Planet. Space Sci. 57 (5–6), 533–540.
Boatwright, B.D., Head, J.W., 2019. Simulating early Mars hydrology with the MARSSIM landform evolution model: new insights from an integrated system of precipitation, infiltration, and groundwater flow. Planet. Space Sci. 171, 17–33.
Conway, S.J., de Haas, T., Harrison, T.N., 2019. Martian gullies: a comprehensive review of observations, mechanisms and insights from Earth analogues. Geol. Soc. Lond., Spec. Publ. 467 (1), 7–66.
Davila, A.F., Warren-Rhodes, K., DiRuggiero, J., 2021. The Atacama Desert: a window into late Mars surface habitability?. In: Soare, R., Conway, S., Williams, J.-P., Oehler, D. (Eds.), Mars Geological Enigmas From the Late Noachian Epoch to the Present Day. Elsevier, pp. 333–356.
Fukushi, K., Sekine, Y., Sakuma, H., Morida, K., Wordsworth, R., 2019. Semiarid climate and hyposaline lake on early Mars inferred from reconstructed water chemistry at Gale. Nat. Commun. 10 (1), 1–11.
Ghezzehei, T.A., Kneafsey, T.J., Su, G.W., 2007. Correspondence of the Gardner and van Genuchten–Mualem relative permeability function parameters. Water Resour. Res. 40, W10417.
Goldspiel, J.M., Squyres, S.W., 2011. Groundwater discharge and gully formation on Martian slopes. Icarus 211 (1), 238–258.
Grimm, R.E., Harrison, K.P., Stillman, D.E., 2014. Water budgets of Martian recurring slope lineae. Icarus 233, 316–327.
Grimm, R.E., Harrison, K.P., Stillman, D.E., Kirchoff, M.R., 2017. On the secular retention of ground water and ice on Mars. J. Geophysical Res. Planets 122 (1), 94–109.
Groemer, G., Gruber, S., Uebermasser, S., Soucek, A., Lalla, E.A., Lousada, J., Sams, S., Sejkora, N., Garnitschnig, S., Sattler, B., Such, P., 2020. The AMADEE-18 Mars analog expedition in the Dhofar region of Oman. Astrobiology 20 (11), 1276–1286.
Hobbs, S.W., Paull, D.J., Clarke, J.D.A., 2014. A hydrological analysis of terrestrial and Martian gullies: implications for liquid water on Mars. Geomorphology 226, 261–277.
Horvath, D.G., Andrews-Hanna, J.C., 2021. The hydrology and climate of Mars during the sedimentary infilling of Gale crater. Earth Planet. Sci. Lett. 568, 117032.
Horvath, D.G., Andrews-Hanna, J.C., Newman, C.E., Mitchell, K.L., Stiles, B.W., 2016. The influence of subsurface flow on lake formation and north polar lake distribution on Titan. Icarus 277, 103–124.
Hunt, B.W., 1973. Seepage from shallow reservoir. J. Hydraulics Division ASCE 99 (1), 23–30.
Ilyinsky, N.B., Kacimov, A.R., Yakimov, N.D., 1998. Analytical solutions of seepage theory problems. Inverse methods, variational theorems, optimization and estimates (A review). Fluid Dynam. 33 (2), 157–168.
Kacimov, A., Obnosov, Y.V., Šimůnek, J., 2020. Seepage to ditches and topographic depressions in saturated and unsaturated soils. Adv. Water Resour.. https://doi.org/10.1016/j.advwatres.2020.103732.
Kacimov, A.R., Al-Shukaili, A., Al-Mayahi, A., Al-Maktoumi, A., 2021. Triangular ditch of fastest infiltration into porous substratum. J. Irrigation Drainage ASCE 147 (7), 06021002.
Kereszturi, A., Möhlmann, D., Berczi, S., Ganti, T., Horvath, A., Kuti, A., Sik, A., Szathmary, E., 2010. Indications of brine related local seepage phenomena on the northern hemisphere of Mars. Icarus 207 (1), 149–164.
Kochel, R.C., Piper, J.F., 1986. Morphology of large valleys on Hawaii—evidence for groundwater sapping and comparisons with Martian valleys. J. Geophys. Res. 91 (B13), E175–E192.
Lark, L.H., Huber, C., Head, J.W., 2020. Anomalous Recurring Slope Lineae on Mars: Implications for Formation Mechanisms. Icarus, p. 114129.
Luo, W., Grudzinski, B., Pederson, D., 2011. Estimating hydraulic conductivity for the Martian subsurface based on drainage patterns—A case study in the Mare Tyrrhenum Quadrangle. Geomorphology 125 (3), 414–420.
Mahato, R.K., Dey, S., 2020. Hydraulics of seepage from trapezoidal channels. J. Hydraulic Eng. ASCE (12), 146. 04020083.
Malin, M.C., Carr, M.H., 1999. Groundwater formation of Martian valleys. Nature 397 (6720), 589–591.
Malin, M.C., Edgett, K.S., 2000. Evidence for recent groundwater seepage and surface runoff on Mars. Science 288 (5475), 2330–2335.
Marra, W.A., Braat, L., Baar, A.W., Kleinhans, M.G., 2014. Valley formation by groundwater seepage, pressurized groundwater outbursts and crater-lake overflow in flume experiments with implications for Mars. Icarus 232, 97–117.
Marra, W.A., McLelland, S.J., Parsons, D.R., Murphy, B.J., Hauber, E., Kleinhans, M.G., 2015. Groundwater seepage landscapes from distant and local sources in experiments and on Mars. Earth Surface Dynam. 3 (3), 389–408.
Michalski, J.R., Cuadros, J., Niles, P.B., Parnell, J., Rogers, A.D., Wright, S.P., 2013. Groundwater activity on Mars and implications for a deep biosphere. Nat. Geosci. 6 (2), 133–138.
Mukherjee, S., Singh, D., Singh, P., Roy, N., 2020. Morphological and morphometric analysis of a topographic depression near Huygens basin, Mars: identification of a putative endorheic playa. Geomorphology 351, 106912.
Petroff, A.P., Devauchelle, O., Seybold, H., Rothman, D.H., 2013. Bifurcation dynamics of natural drainage networks. Philos. Trans. R. Soc. A Math. Phys. Eng. Sci. 371, 20120365. 2004.
Philip, J.R., 1990. How to avoid free boundary problems. In: Hoffman, K.H., Sprekels, J. (Eds.), Free Boundary Problems: Theory and Applications. Longman, New York, pp. 193–207.
Philip, J.R., 1992. Falling-head ponded infiltration with evaporation. J. Hydrol. 138 (3–4), 591–598.
Polubarinova-Kochina, P.Y., 1962. 1977. Theory of Ground Water Movement. 2nd ed. Princeton Univ. Press, Princeton. Nauka, Moscow (in Russian).
Radcliffe, D., Šimůnek, J., 2010. Soil Physics with HYDRUS: Modeling and Applications. CRC Press, Taylor & Francis Group, Boca Raton.
Rehbinder, G., Isaksson, A., 1998. Large-scale flow of groundwater in Swedish bedrock. An analytical calculation. Adv. Water Resour. 21 (6), 509–522.
Reynolds, W.D., 2015. A generalized variable-head borehole permeameter analysis for saturated, unsaturated, rigid or deformable porous media. Eng. Geol. 185, 10–19.
Salese, F., Pondrelli, M., Neeseman, A., Schmidt, G., Ori, G.G., 2019. Geological evidence of planet-wide groundwater system on Mars. J. Geophysical Res. Planets 124 (2), 374–395.
Sasidharan, S.A.B., Šimůnek, J., DeJong, B., Kraemer, S.R., 2018. Evaluating drywells for stormwater management and enhanced aquifer recharge. Adv. Water Resour. 116, 167–177. https://doi.org/10.1016/j.advwatres.2018.04.003.
Šimůnek, J., Šejna, M., van Genuchten, M.T., 2018. New features of version 3 of the HYDRUS (2D/3D) computer software package. J. Hydrol. Hydromechanics 66 (2), 133–142. https://doi.org/10.1515/johh-2017-0050.
Sophocleous, M., 2002. Interactions between groundwater and surface water: the state of the science. Hydrogeol. J. 10 (1), 52–67.
Strack, O.D.L., 2017. Analytical Groundwater Mechanics. Cambridge Univ, Press, New York.
Toller, E.A., Strack, O.D., 2019. Interface flow with vertically varying hydraulic conductivity. Water Resour. Res. 55 (11), 8514–8525.
Warrick, A.W., Zhang, R., 1987. Steady two-and three-dimensional flow from saturated to unsaturated soil. Adv. Water Resour. 10 (2), 64–68.
Weir, G.J., 1986. Steady infiltration from large shallow ponds. Water Resour. Res. 22 (10), 1462–1468.
Woessner, W.W., 2020. Groundwater-Surface Water Exchange. Groundwater Project, Guelph.
Wolfram, S., 1991. Mathematica. A System for Doing Mathematics by Computer. Addison-Wesley, Redwood City.
Wooding, R.A., 1968. Steady infiltration from a shallow circular pond. Water Resour. Res. 4 (6), 1259–1273.
Wray, J.J., 2021. Contemporary liquid water on Mars?. Annu. Rev. Earth Planet. Sci. 49, 141–171.
Касимов, А.Р., Тартаковский, Д.М., 1993. Оценка времени миграции трассера в потоке грунтовых вод. Журнал Вычислительной Математики и Математической Физики 33 (11), 1751–1759. (in Russian). Engl. translation: Kasimov, A.R., and Tartakovsky, D.M., 1993. Estimation of tracer migration time in ground water flow. Comput. Math. Math. Phys., 33(11), 1535–1541.